



## Effects of Au@Ag core-shell nanostructure with alginate coating on male reproductive system in mice

Mahsa Nazari<sup>a</sup>, Ronak Shabani<sup>b</sup>, Marziyeh Ajdary<sup>c</sup>, Mohsen Ashjari<sup>d</sup>, Reza Shirazi<sup>e</sup>, Azam Govahi<sup>c</sup>, Fatemeh Kermanian<sup>f</sup>, Mehdi Mehdizadeh<sup>b,\*</sup>

<sup>a</sup> Department of Anatomy, School of Medicine, Iran University of Medical Sciences, Tehran, Iran

<sup>b</sup> Reproductive Sciences and Technology Research Center, Department of Anatomy, Iran University of Medical Sciences, Tehran, Iran

<sup>c</sup> Endometriosis Research Center, Iran University of Medical Sciences (IUMS), Tehran, Iran

<sup>d</sup> Chemical Engineering Department, Faculty of Engineering, University of Kashan, Kashan, Iran

<sup>e</sup> Department of Anatomy, School of Medical Sciences, Medicine & Health, UNSW Sydney, Sydney, Australia

<sup>f</sup> Department of Anatomy, Alborz University of Medical Sciences, Karaj, Iran

### ARTICLE INFO

Handling Editor: Prof. L.H. Lash

#### Keywords:

Nanostructures  
Semen analysis  
Apoptosis  
Autophagy  
Fertilization  
Testicular tissue

### ABSTRACT

Despite the widespread use of silver nanoparticles (NPs), these NPs can accumulate and have toxic effects on various organs. However, the effects of silver nanostructures (Ag-NS) with alginate coating on the male reproductive system have not been studied. Therefore, this study aimed to investigate the impacts of this NS on sperm function and testicular structure. After the synthesis and characterization of Ag-NS, the animals were divided into five groups ( $n = 8$ ), including one control group, two sham groups (received 1.5 mg/kg/day alginate solution for 14 and 35 days), and two treatment groups (received Ag-NS at the same dose and time). Following injections, sperm parameters, apoptosis, and autophagy were analyzed by the TUNEL assay and measurement of the mRNA expression of *Bax*, *Bcl-2*, *caspase-3*, *LC3*, and *Beclin-1*. Fertilization rate was assessed by in vitro fertilization (IVF), and testicular structure was analyzed using the TUNEL assay and hematoxylin and eosin (H&E) staining. The results showed that the NS was rod-shaped, had a size of about 60 nm, and could reduce sperm function and fertility. Gene expression results demonstrated an increase in the apoptotic markers and a decrease in autophagy markers, indicating apoptotic cell death. Moreover, Ag-NS invaded testicular tissues, especially in the chronic phase (35 days), resulting in tissue alteration and epithelium disintegration. The results suggest that sperm parameters and fertility were affected. In addition, NS has negative influences on testicular tissues, causing infertility in men exposed to these NS.

**Abbreviations:** AA, Ascorbic acid; AgNO<sub>3</sub>, Silver nitrate; Ag-NPs, silver nanoparticles; AMPkinase, 5' adenosine monophosphate-activated protein kinase; ANOVA, Analysis of variance; Atg3, Autophagy related 3; BAX, Bcl-2-associated X protein; Bcl-2, B-cell lymphoma 2; BTB, Blood-testes barrier; cDNA, Complementary DNA; CSNs, Core-shell nanostructures; CTAB, Cetyltrimethylammonium bromide; ct, cycle threshold; DLS, Dynamic light scattering; dUTP, Deoxyuridine triphosphate; DW, Distilled water; FTIR, Fourier transform infrared spectroscopy; FYN kinase, Proto-oncogene tyrosine-protein kinase; HAuCl<sub>4</sub>, Tetrachloroauric acid trihydrate; hCG, human chorionic gonadotropin; HR-TEM, High-resolution transmission electron microscopy; H<sub>2</sub>SO<sub>4</sub>, Sulphuric acid; ICP-MS, Inductively coupled plasma mass spectrometry; IgE, Immunoglobulin E; IL, Interleukins; IU, International Unit; NaBH<sub>4</sub>, Sodium borohydride; NaOH, Sodium hydroxide; NIH, National Institutes of Health; NMRI, Naval Medical Research Institute; NMs, Nanomaterials; NRs, Nano rods; OD, Optical density; PBS, Phosphate-buffered saline; PdI, Polydispersity index; PI, Propidium Iodide; PMSG, Pregnant Mare Serum Gonadotropin; q RT-PCR, Quantitative real time - polymerase chain reaction; ROS, Reactive oxygen species; rpm, Rotations Per Minute; SD, standard deviation; SERS, Surface enhanced Raman scattering; SNRs, Silver Nano rods; SSCs, Spermatogonial stem cells; TDT, Terminal deoxynucleotidyl transferase; TGA, Thermal gravimetric Analysis; TGF-β, Transforming growth factor; TUNEL, Terminal deoxynucleotidyl transferase dUTP nick end labeling.

\* Correspondence to: Reproductive Sciences and Technology Research Center, Department of Anatomy, Iran University of Medical Sciences, Tehran 15875-1454, Iran.

E-mail address: [Mehdizadeh.m@iums.ac.ir](mailto:Mehdizadeh.m@iums.ac.ir) (M. Mehdizadeh).

<https://doi.org/10.1016/j.toxrep.2023.01.003>

Received 26 November 2022; Accepted 7 January 2023

Available online 10 January 2023

2214-7500/© 2023 The Authors. Published by Elsevier B.V. This is an open access article under the CC BY-NC-ND license (<http://creativecommons.org/licenses/by-nc-nd/4.0/>).

## 1. Introduction

Spermatogenesis in mammals is a complicated developmental process in the germinal epithelium of the testicular tubules and results in the formation of haploid spermatozoa [1]. All steps of spermatogenesis, including mitotic and meiotic divisions and spermiogenesis [2], require coordinated interplay between Sertoli, germ, and Leydig cells [3]. Half of the genome of the embryo is provided by the sperm, which contributes significantly to normal fertilization. In addition, studies have demonstrated that approximately 60% of men with infertility problems have damaged DNA and high sperm DNA fragmentation, leading to decreased fertility rate and lower embryo quality [4]. Male infertility is a severe health disorder worldwide [5], the rate of which has augmented 2–3 times in recent years compared to the 1960 s [6], and sperm count and motility declined significantly during 1973–2011 [7]. This problem can be caused by both genetic and environmental factors [5]. Studies have shown that environmental pollutants play an important role in these phenomena [6]. Sperm DNA fragmentation of infertile men is significantly higher than fertile men [5].

Apoptosis is a conserved method of cell death with different biochemical and genetic pathways that remove redundant cells and play a vital role in the homeostasis of normal tissues [8,9]. This process is crucial for the growth and proliferation of cells, development, and well-being. Autoimmune disorders, cancer, and viral diseases might result from defective or inhibited apoptosis. Therefore, studies related to apoptosis aim to understand molecular and regulatory mechanisms, especially Bcl-2 family proteins, which are the major regulatory groups [10]. Autophagy is a protected catabolic process responsible for the nonspecific destruction of long-lived proteins, waste products, and damaged cellular components. This procedure occurs as part of daily cellular activities in response to metabolic stress, hypoxia, or starvation and is essential for maintaining normal cellular function in some diseases, such as cancer [11]. Interaction between these two biological processes allows these pathways to be regulated simultaneously [12].

Nanotechnology is concerned with the synthesis and use of particles with a diameter of 1–100 nm, regarded as nanomaterials (NMs), which are used to diagnose and treat diseases [13]. Precious metal nanoparticles (NPs) have received much attention and interest, and silver is the most commonly used NP in many research areas [14]. Because of their unique properties, the Ag-NPs are used in manufacturing consumer and medical products. These applications include food containers, room sprays, washing machines, toys, water filters, cosmetics, dental alloys, wound dressings, implant surfaces, catheter coatings, and drug delivery in cancer therapies [3,15]. Various methods produce NMs in various shapes, such as spheres, cubes, branched structures, stars, ellipsoids, wires, and rods [16,17]. Nano-rods (NRs) are nanoscale structures in which one dimension is larger than the other, and their aspect ratio (length/diameter) is less than 10. Among various nanostructures, silver NRs have received special attention because of their incomparable properties [17], enabling them to be used in various fields, namely biological imaging, electronics, sensing, catalysis, drug delivery, and cancer therapy [16]. Core-shell nanostructures (CSNs) consist of an inner layer of one substance (Au core) and an outer layer of another substance (Ag shell), forming a hybrid structure [18]. Careful shell selection improves the properties of nanostructures, such as electrical, optical, and magnetic properties, functionality, dispersibility, and stability [19,20]. Some important applications of core/shell nanostructures are catalysis [21,22], cell labeling [23], targeted and controlled drug release [24], bioimaging [25], and tissue engineering [24].

The increasing use of NMs leads to augmented human exposure, which necessitates a thorough analysis of their potential toxicity and the identification of their biological interactions [17]. According to the literature, people may be exposed to Ag NPs via oral ingestion (food, water, and drugs), skin contact, bloodstream (drug delivery devices), and inhalation [3,26]. Ag NPs reduce cell viability by promoting reactive oxygen species production (ROS), DNA damage, increased

mitochondrial membrane permeability, and cell apoptosis [27]. Despite the superior properties of anisotropic silver NPs over spherical particles, it is essential to evaluate the biocompatibility and toxicity of the anisotropic Ag NPs [28]. One strategy used by researchers to modify the chemical and physical properties and improve the biocompatibility of NM is using chitosan, gelatin, sodium alginate, and other polymeric materials [17].

Most research has investigated the effect of spherical silver NPs on the male reproductive system. No study focused on silver NRs and their impacts on male mice. Therefore, the aim of the present study was to investigate the toxicity of Au@Ag core-shell NRs with a biocompatible coating (alginate) on sperm parameters. In addition, the effect of Ag NRs over different periods (14 and 35 days) on the expression of apoptotic and autophagy markers was studied, and the fertilization rate was assessed by IVF.

## 2. Materials and methods

### 2.1. Reagents

Tetrachloroauric acid trihydrate ( $\text{HAuCl}_4 \cdot 0.3 \text{H}_2\text{O}$ , 99.9% trace metal basis) and ascorbic acid (AA,  $\geq 99.7\%$ ) were obtained from Sigma-Aldrich (USA). Silver nitrate ( $\text{AgNO}_3$ ,  $\geq 99.8\%$ ), sodium borohydride ( $\text{NaBH}_4$ , 99.99%), cetyltrimethylammonium bromide (CTAB, 99.9%), sodium hydroxide (NaOH, 97%), and sulphuric acid ( $\text{H}_2\text{SO}_4$ ) were purchased from Merck (Germany). All chemicals were used without additional purification. All containers were washed with aqua regia ( $\text{HCl}/\text{HNO}_3$ , volume ratio 3:1) and distilled water (DW).

### 2.2. Synthesis of nanostructure

Au-NRs were produced using the seed-mediated growth method based on a previous report [29].

#### 2.2.1. Gold seed solution

A volume of 0.1 ml of ice-cold  $\text{NaBH}_4$  solution (0.01 M), as a reducing agent, was added to 0.0417 ml of  $\text{HAuCl}_4$  (0.5 mM) and 1.25 ml of CTAB solutions (0.2 M) with vigorous stirring. After 2 min, a brownish-yellow solution was obtained and stored at room temperature for 5–6 h.

#### 2.2.2. Gold growth solution

An aqueous solution containing 500 ml of CTAB (0.2 M) was prepared. Afterwards, 25 ml of  $\text{HAuCl}_4$  (0.001 M), 4.5 ml of  $\text{AgNO}_3$  (0.004 M, fresh), 10 ml of  $\text{H}_2\text{SO}_4$  (0.5 M), 4 ml of ascorbic acid (0.0788 M, fresh), and 1.25 ml of seed solution were added under stirring. The solution was kept at 30 °C in all experiments and was used after 12 h. When ascorbic acid was added as a weak reducing agent, a change was observed in the color of the solution from dark yellow to colorless. The color of the prepared solution changed slowly and became after 10–20 min

#### 2.2.3. Silver shell

In order to generate the silver shell on the surface of Au NRs, the synthesized Au NRs were centrifuged twice (12,000 rpm, 10 min), and the supernatant was removed. Next, 30 ml of Au NRs, 1.95 ml of  $\text{AgNO}_3$  (0.01 M), 3 ml of ascorbic acid (0.1 M), and 0.3 ml of NaOH (1 M) were added to 90 ml of CTAB solution (0.1 M). In this step, the solution color varies depending on the concentration of silver (light gray, green, blue-green, or purple). In the present study, the solution was green.

#### 2.2.4. Alginate coating

The Au@Ag core-shell NR solution was centrifuged at 6000 rpm for 10 min. After removing the supernatant, alginate solution 1% (0.25 g alginate+25 ml DW) was added to the resulting precipitate and was resuspended by sonication. This procedure (centrifugation, addition,

and sonication) was repeated, and the final solution was used for injection.

### 2.3. Nanostructure characterization

A HACH (UK) UV–visible spectrophotometer was used to record the UV–visible absorption of Au NR, Au@Ag core-shell NR, and Au@Ag core-shell NR with alginate coating in the wavelength range of 300–900 nm. Fourier transform infrared spectroscopy (FTIR) (PerkinElmer, Frontier, USA) confirmed the change in surface nanostructure coating from CTAB to alginate in the range of 400–4000  $\text{cm}^{-1}$ . A Philips PW1730 (Netherlands) X-ray diffractometer with  $\text{K}\alpha$  ( $\lambda = 1.54059$  nm wavelength) in the  $2\theta$  range of  $20^\circ - 90^\circ$  was applied to record the X-ray diffraction (XRD) patterns of the nanostructures.

The size distribution and shape of the core-shell nanostructure, as well as the thickness of the silver shell, were measured by high-resolution transmission electron microscopy (HR-TEM) using a 200 KV HR-TEM (TECNAL F20, FEI, USA). Hydrodynamic particle size and zeta potential were determined by dynamic light scattering (DLS, NANO-flex, Germany). The Inductively coupled plasma mass spectrometry (ICP-MS, Varian - 573 Radial) was utilized to determine the concentration of silver in the nanostructure solution. Afterwards, 25 ml of the silver solution was centrifuged at 6000 rpm for 10 min. After removing the supernatant, 1 cc of aqua regia and then 29 ml of DW were added to the precipitate. The final clear solution (30 ml) was used to determine the concentration.

### 2.4. Animal groups and experimental design

A total of 40 adult male Naval Medical Research Institute (NMRI) mice aged 5 weeks and weighing 25–30 g were studied. The mice were purchased from the Centre of Experimental and Comparative Studies, Iran University of Medical Sciences, Iran, and all experiments were performed according to the National Institutes of Health (NIH) guidelines and were approved by the Animal Ethics Committee of Iran University of Medical Sciences, Tehran, Iran (IR.IUMS.FMD.REC.1398.433). The animals were kept in clean cages during the experiment under controlled light (12 h light, 12 h dark) with controlled temperature ( $22-25^\circ\text{C}$ ) and free access to water and food.

The mice were randomly divided into five groups of eight subjects. One control group received no substances during the experiment. Two sham groups received alginate solution at a 1.5 mg/kg/day dose via intraperitoneal injection for 14 (Al 14) and 35 (Al 35) days, and two treatment groups were treated with nanostructure solution at the same dose and time point (Ag 14 and Ag 35). The mice were sacrificed one day after the last treatment. The cauda epididymis and testes were removed from each animal and were used for the following experiments (Fig. 1).

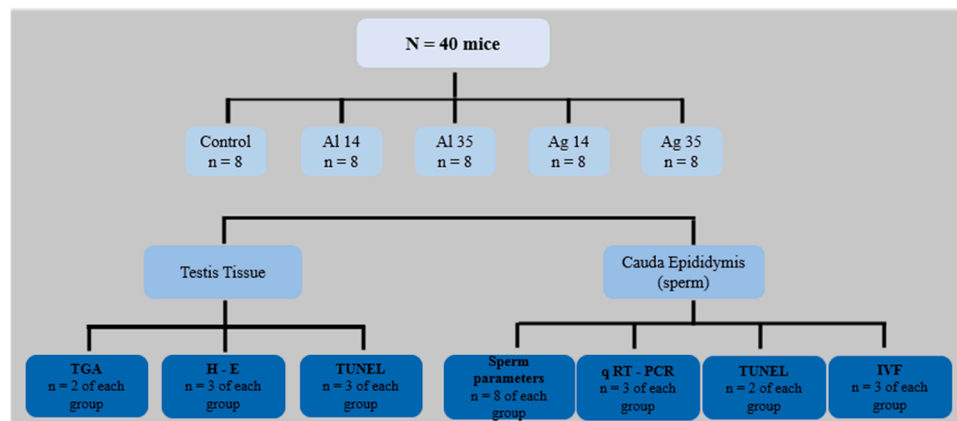


**Fig. 1.** Study design. Five groups of 8 mice each participated in the study. The first group received no material and served as a control group. The second and third groups received 1.5 mg/kg/day alginate solution (Al) for 14 and 35 days, respectively, and served as sham groups. The fourth and fifth groups received Ag nanostructure solution (Ag) at the same dose and for the same time and served as treated groups. One day after the last injection, the mice were sacrificed and the cauda epididymis of each mouse was collected for sperm analysis, evaluation of gene expression, apoptosis, and fertilization rate. Testicular tissue was also collected for apoptosis and histopathological studies. TGA: Thermal gravimetric analysis; IVF: In vitro fertilization.

### 2.5. Sperm parameters

The cauda epididymis was cut off at the lower pole of the testis and was placed in 1 ml of Ham's F10 culture medium (Bioidea, Iran). Ham's F10 medium containing 10% bovine serum albumin (BSA) should be incubated at  $37^\circ\text{C}$  and 5%  $\text{CO}_2$  pressure for at least 4 h before collection. Next, the dishes were incubated with the sperm suspension for 15 min to make the sperm swim out. Count ( $10^6/\text{ml}$ ), motility (%), viability (%), and morphology (%) were assessed for 200 spermatozoa according to the guidelines of the World Health Organization [30]. Briefly, count and motility were determined using a hemocytometer. Samples were analyzed with a light microscope ( $\times 40$  magnification), and ten lamellar fields were examined. Based on the instructions of WHO, spermatozoa were divided into progressive motile, non-progressive motile (total motility expressed as a percentage), and immotile [31,32].

Eosin and Papanicolaou stains were used to evaluate sperm viability and morphology, respectively [33].

### 2.6. Isolation of RNA, synthesis of cDNA, and q RT-PCR

The expression of apoptosis (*Bax*, *Bcl-2*, and *Caspase-3*) and autophagy (*Beclin-1* and *LC3*) genes were assessed by real-time PCR. To achieve this purpose, total RNA in spermatozoa was extracted by TRIzol (Millipore Sigma, Sigma-Aldrich, USA) and chloroform. RNA concentration and purity were measured using the Nano-Drop instrument (Thermo Fisher Scientific Inc., Wilmington, USA) at the optical density (OD) of 260/280 nm and were transcribed into complementary DNA (cDNA) using a cDNA synthesis kit (Fermentas Kit, Thermo Fisher Scientific, USA). The synthesized cDNA was used to perform q RT-PCR (Corbett RESEARCH, Australia) with specific primers. The final volume of  $10\ \mu\text{l}$  contained 5 pmol of specific forward primer, 5 pmol of specific reverse primer, 250 ng of synthesized cDNA, and SYBR Green/ROX dye solution (25:1 vol ratio). Normalization of mRNA levels was conducted by the  $\beta$ -actin expression level, and the  $2^{-\Delta\Delta\text{Ct}}$  method was used for data analysis [34]. The used primer sequences are listed in Table 1.

### 2.7. TUNEL assay

The TUNEL assay was performed to detect spermatozoa apoptosis. Tunnel staining is based on the ability of the enzyme terminal deoxynucleotidyl transferase to introduce labeled dUTP (deoxyuridine triphosphate) to the free end of 3' hydroxyl [35]. First, sperm smears were fixed with paraformaldehyde 4% in phosphate-buffered saline (PBS) at  $\text{pH} = 7.4$  and  $15-25^\circ\text{C}$  for 20 min. Next, the slides were washed and incubated with PBS (30 min) and blocking solution, respectively. After rinsing with PBS, the cells were incubated for 1 h in a dark, humid

**Table 1**  
Primer sequences used in Real-time PCR.

Gene	Sequence (5' → 3')	Length	Tm	PCR product size (bp)
<i>β-actin</i>	Forward:	20	58	90
	CAAGATCATTGCTCCTCTG	19	57	
	Reverse:			
	ATCCACATCTGCTGGAAGG			
<i>Bax</i>	Forward:	20	58	118
	AGGATGATTGCTGACGTGGA	22	62	
	Reverse:			
	CAAAGTAGAAGAGGGCAACCAC			
<i>Bcl-2</i>	Forward:	22	62	104
	GGTGCTCTTGAGATCTCTGGTT	22	62	
	Reverse:			
	AGGTGGAGGAAAATCAGGAGG			
<i>Caspase3</i>	Forward:	21	59	97
	AGGCTGACTTCTGTATGCTT	20	58	
	Reverse:			
	ATGCTGCAAAGGGACTGGAT			
<i>Beclin-1</i>	Forward:	22	60	106
	TTTTAGACCAGCTGGACACTCA	23	61	
	Reverse:			
	TGCTCACTGTATCCTCATTTCAT			
<i>Map1lc3b</i>	Forward:	22	62	70
	GACGGCTTCTGTACATGGTTT	22	62	
	Reverse:			
	TGGAGTCTTACACAGCCATTGC			

environment with a 50  $\mu$ l TUNEL mixture. Finally, slides were washed with PBS and were viewed after mounting with a fluorescence microscope (Olympus Co., Tokyo, Japan) at  $\times 100$  magnification [36]. Spermatozoa with light and pale green colors are considered TUNEL-positive (DNA fragmentation) and -negative (normal), respectively.

## 2.8. In vitro fertilization

### 2.8.1. Follicular stimulation and oocytes collection

On the first day, the superovulation of female mice aged 4–5 weeks old was carried out by injecting 5 IU of pregnant mare serum gonadotropin (PMSG, Folligon, Netherlands) intra-peritoneally at about 6–7 pm. After 48 h, 5 IU of human chorionic gonadotropin (hCG, Darou Pakhsh, Iran) was injected. After 15–17 h, the mice were sacrificed under anesthesia, the fallopian tubes of each side were removed, and the oocytes with cumulus oophorus were transferred to the IVF Medium under mineral oil [37].

### 2.8.2. Sperm preparation

For sperm preparation, mouse cauda epididymis were dissected, cut, and placed in Ham's F10 medium /10% BSA. The Petri dishes were incubated at 37 °C for 15 min to swim out the sperm. The sperm suspension was then centrifuged at 3000 rpm for 5 min, and the resulting pellet was resuspended in 0.5 ml of Ham's F10/BSA medium and incubated at 37 °C for 1 h for capacitation [38].

### 2.8.3. Fertilization

For each mouse, 15 oocytes (total number of oocytes = 225) were placed in 50  $\mu$ l drops of IVF medium (each drop contained three oocytes). One million spermatozoa were inseminated into each drop, and the Petri dishes were incubated for approximately 6 h. Fertility success was determined by stereomicroscopy and observation of the pronucleus [37].

## 2.9. Thermal gravimetric analysis (TGA)

Thermogravimetric analysis (Q600, TA, USA) was performed to confirm the nanostructures' penetration into the testicular tissue. The left testis of each animal was heated at a heating rate of 10 °C/min under N<sub>2</sub> (25–800 °C).

## 2.10. Testes tissue histological evaluation and TUNEL assay

The right testes of the animals were immediately fixed in Bouin solution for 72 h. After processing and embedding in paraffin wax, 5  $\mu$ m sections were made using a microtome (Didsabz, DS8402, Iran) and stained with hematoxylin and eosin [13,39]. After preparing 5  $\mu$ m of paraffin sections, deparaffinizing, and dehydrating, the remaining steps were performed according to the protocol of the Kit (Roche, Germany). Samples were incubated with PBS (20 min at room temperature), blocking solution (H<sub>2</sub>O<sub>2</sub> 3% in methanol for 10 min at room temperature), permeabilization solution (DW + Triton + sodium citrate, 15 min at 2–8 °C), and TUNEL mixture (this solution is prepared according to the protocol of the kit in a dark and humid environment during 1 h). Differential staining of nuclei with Propidium Iodide (PI) was also performed. Slides were examined using a fluorescence microscope (Olympus Co., Tokyo, Japan) with a green filter at  $\times 40$  magnification.

## 2.11. Data analysis

The data were analyzed using GraphPad Prism software version 8.0. The normality of the data was assessed by the Kolmogorov–Smirnov test, and then one- and two-way analysis of variance (ANOVA) and Tukey's post-hoc test were used to detect significant differences between variables and groups. Fertilization rate analysis was performed using the chi-square test. The results are expressed as mean  $\pm$  standard deviation (SD), and P-value  $\leq 0.05$  was considered significant.

## 3. Results

### 3.1. Characterization of nanostructure

After each synthesis step, the shape of the resulting NM was confirmed with UV-Vis. The UV-Vis absorption spectra for Au NRs, Au@Ag NRs, and Au@Ag NRs with alginate coating are shown in Fig. 2A. According to this figure, the Au NRs have an intense absorption peak at 841 nm and a less intense peak at 514 nm. The addition of a silver coat results in a redshift and a decrease in the intensity of the peaks, with two peaks indicated at 627 and 486 nm. After the surface was coated with alginate, the intensity of peaks declined sharply at the same wavelengths as before.

To identify the functional groups of the nanostructure, FT-IR spectroscopy was used before and after alginate coating. Fig. 2B presents the results of this analysis. In the diagram demonstrating CTAB, the observed peaks at 3016 cm<sup>-1</sup> represent the N-H stretching band of the trimethylammonium head group of CTAB. Moreover, the peaks at 2918 and 2849 cm<sup>-1</sup> are related to the C-H stretching band. The peaks at 1737, 1487, and 1396 cm<sup>-1</sup> are related to the N-H band of the head group of CTAB, C-H stretching band, and the C-H bending band, respectively. The alginate diagram shows that the detected bands at 2924 cm<sup>-1</sup> correspond to the CH -anomer, at 1591 cm<sup>-1</sup> to the asymmetric -COO- group, at 1401 cm<sup>-1</sup> to the symmetric -COO- group, at 1088 cm<sup>-1</sup> to the O-C-O ring group, and 770 cm<sup>-1</sup> to the guluronic acid residues in the alginate structure.

The XRD spectral pattern of the obtained nanostructures is depicted in Fig. 2C. This pattern demonstrates sharp peaks at  $2\theta = 38.49, 44.84, 64.94,$  and  $78.24$ , which is a reason for the successful synthesis of the nanostructure. Structural analysis revealed that the mentioned peaks are related to the crystal plates (111), (200), (220), and (311), respectively, which correspond to the structural plates of the cubic crystals of the silver face center (Bragg reflections). Peak (111) is more intense than the other peaks, showing that the crystal plates of silver NPs tend to form in this direction.

High-resolution transmission electron microscopy images, shown in Fig. 3A–C, indicate a rod-like nanostructure and a silver coating of about 2.8 nm thickness on gold NRs. The nanostructures are uniform with a suitable rod-core-shell structure. Their length, diameter, and aspect

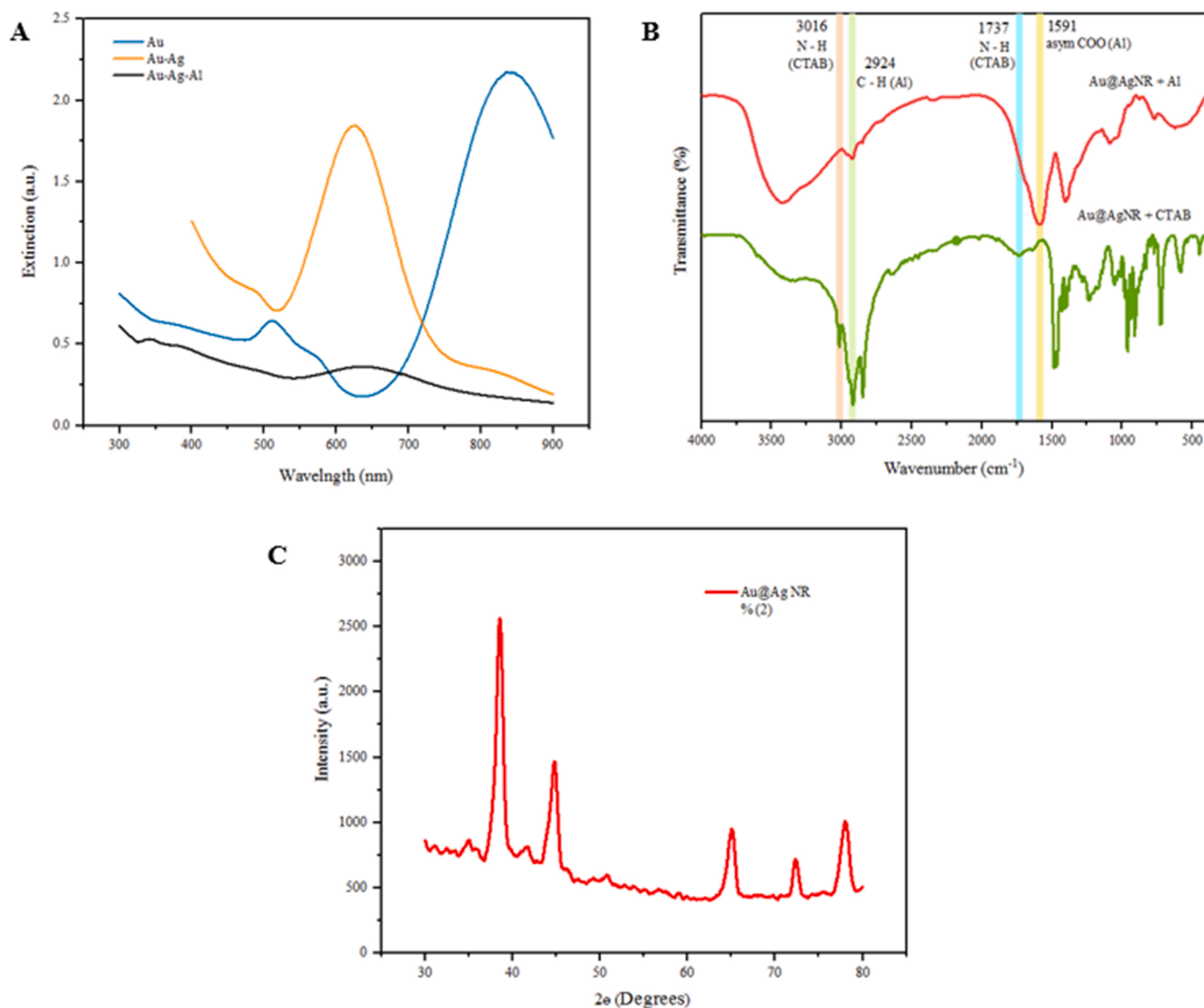


**Fig. 2.** Characterization of nanostructure. (A) UV–visible spectra of Au NRs, Au@Ag NRs, and Au@Ag NRs with alginate coating. (B) FTIR spectra of Au@Ag NRs with CTAB and Au@Ag NRs with alginate coating. (C) XRD analysis of Au@Ag NRs.

ratio are 50–60, 25, and 2.4 nm, respectively. Dynamic light scattering was performed to determine the nanostructures' hydrodynamic size, which yielded approximately 70 nm, consistent with the results obtained by TEM (Fig. 3D). The mean of zeta potential of Au@Ag NS with CTAB and Au@Ag NS with alginate coating was measured to be  $+62.13 \pm 1.87$  mV and  $-62.53 \pm 1.30$  mV, respectively (Fig. 3E). The mean of Ag concentration in the final solution was determined to be 3.27 mg/l by the MMS-01 method.

### 3.2. Sperm parameters

The study of sperm count showed a significant decrease in free sperm in the groups treated with silver nanostructures (14 and 35 days) compared to the other groups. This decrease was accompanied by an increase in sperm aggregation (Fig. 4B-C). Therefore, a significant decrease in sperm count was observed when free sperm were investigated in the treated groups and compared with the control ( $*P < 0.0001$ ) and alginate ( $\#P < 0.0001$ ) groups (Fig. 4A).

It should be noted that the number of progressive sperm and Total motility (progressive and non-progressive sperm) were significantly reduced in the treatment groups compared with the control

( $*P < 0.0001$ ) and sham ( $\#P < 0.0001$ ) groups (Fig. 5A-B).

A significant decrease in sperm viability was evident in the treated groups compared with control ( $*P < 0.0001$ ) and alginate ( $\#P < 0.0001$ ) groups (Fig. 6), there were also statistically significant differences between Ag 14 and 35 and the other groups in the morphological parameters, especially in the coiled tails (Fig. 7A-B).

### 3.3. Gene expression

Assessment of mRNA levels of apoptotic genes showed a significant increase in *Bax* (between Ag35, control, and sham groups) ( $*P = 0.0160$ ) and *caspase-3* (between Ag35, Ag14, and other groups) ( $*P < 0.0001$  for the control group and  $\#P < 0.0001$  for the alginate groups) and a significant decrease in *Bcl-2* in the Ag 14 and Ag 35 groups versus the control ( $*P < 0.0001$ ) and sham ( $\#P < 0.0001$ ) groups. There are no significant differences between the two treatment groups (Fig. 8A-C). The mRNA levels of LC3 and Beclin-1 genes (autophagic markers) significantly decreased in Ag14 and Ag35 groups compared with control ( $*P < 0.0001$ ) and alginate groups ( $\#P < 0.0001$ ), as shown in Fig. 8D-E, respectively.

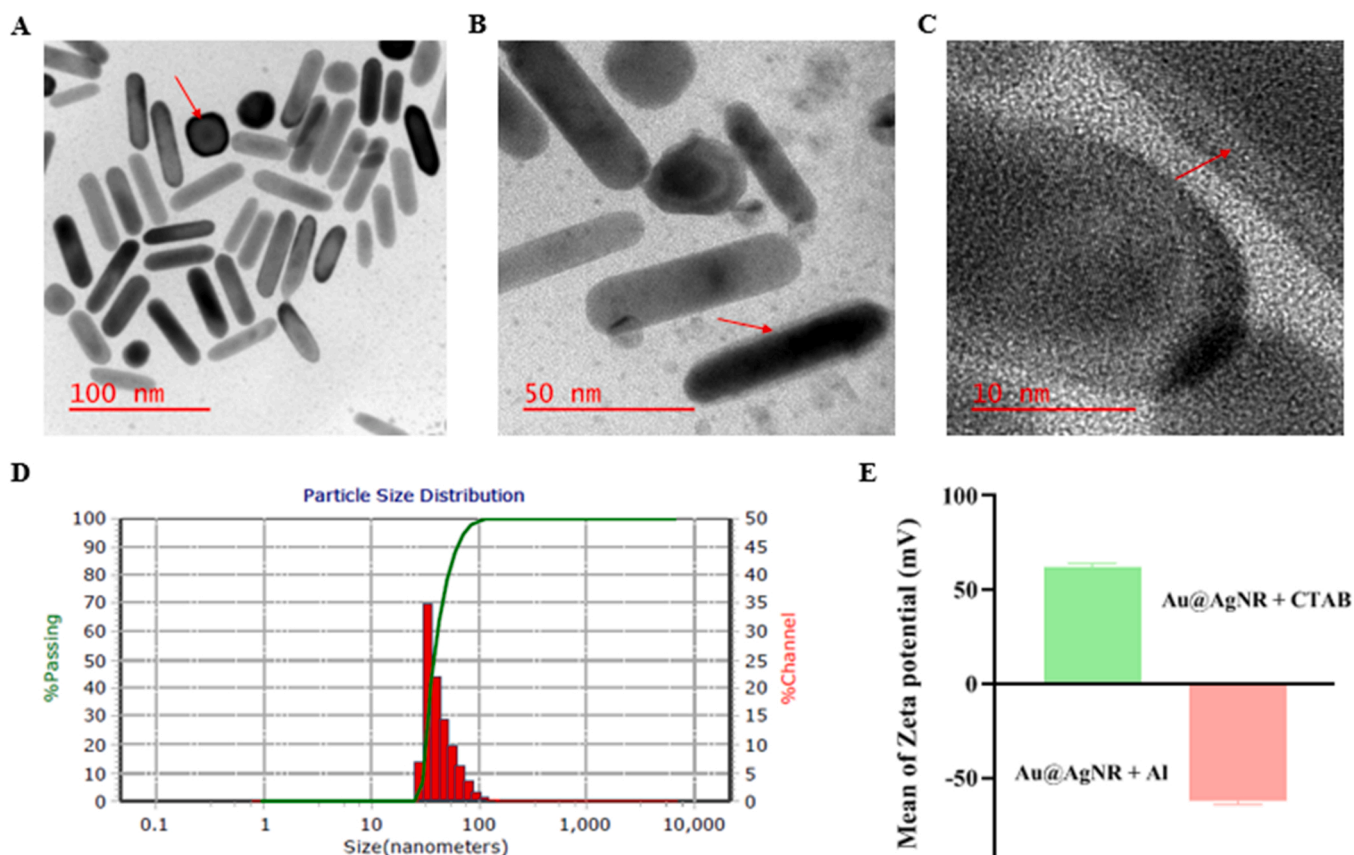


Fig. 3. Characterization of nanostructure. (A–C) High-resolution TEM images with different magnifications. The arrows indicate the silver shell. (D) Dynamic light scattering (DLS) diagram of nanostructure with PdI: 2.715. (E) The zeta potential of Au@Ag NRs with CTAB and Au@Ag NRs with alginate coating.

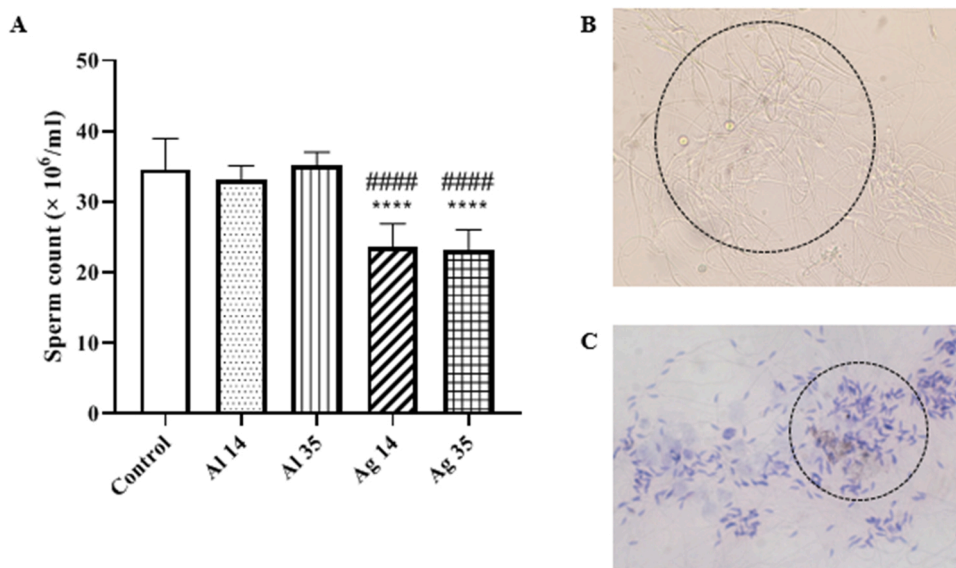


Fig. 4. The effect of nanostructure on sperm count in the studied groups. (A) Comparison of sperm count in the Ag, sham and control groups. Vast sperm aggregation observed under the microscope (B) without staining ( $\times 40$ ) and (C) with Papanicolaou staining ( $\times 10$ ). All results were expressed as mean  $\pm$  SD ( $n = 8$ ). The \* stands for the values against the control group and # stands for the values against the sham groups. The \*\*\*\* and ##### show  $P < 0.0001$ .

### 3.4. Sperm TUNEL assay

Qualitative evaluation of the sperm TUNEL assay showed an increase in light green sperm cells, termed TUNEL positive, in the treated groups compared to the other groups, confirming the apoptotic gene expression

results (Fig. 9).

### 3.5. Fertilization rate

Due to the strong sperm aggregation and reduced motility in the

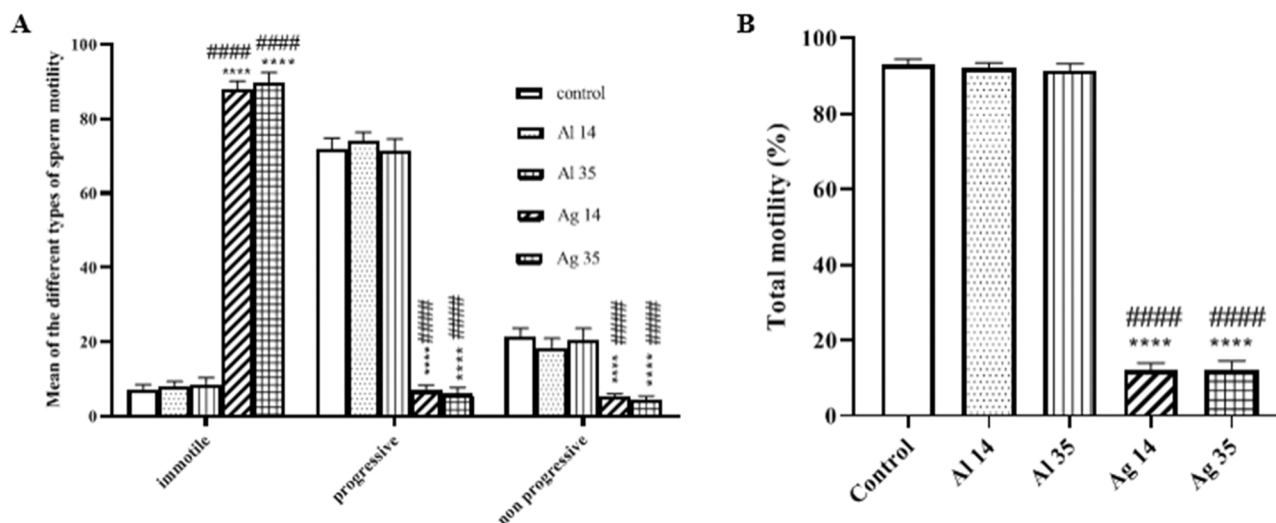


**Fig. 5.** The effect of nanostructure on sperm motility in the studied groups. (A) Comparison of the different types of motility in the experimental groups. (B) Total motility. All results were expressed as mean  $\pm$  SD ( $n = 8$ ). \* \* \* \*  $P < 0.0001$  compared with control group and #####  $P < 0.0001$  compared with sham groups.

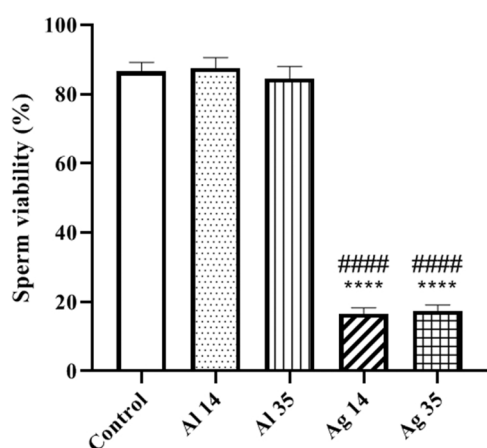


**Fig. 6.** Comparison of sperm viability in the studied groups. All results were expressed as mean  $\pm$  SD ( $n = 8$ ). The \* represents the values compared with the control group and the # represents the values compared with the sham groups. The \* \* \* \* and ##### show  $P < 0.0001$ .

treated groups, the fertilization rate differed significantly between these groups and the control (\* $P < 0.0001$ ) and sham (# $P < 0.0001$ ) groups. (Fig. 10A-C).

### 3.6. Thermal gravimetric analysis

Fig. 11A-B show the weight loss of testes in the Ag 14 and Ag 35 groups, respectively. The body tissue contains organic materials that disperse at high temperatures. Diagram B demonstrates that the weight of the testes decreases rapidly due to water evaporation, shrinks at 100 °C to half, and then stagnates. This weight stability remains constant with an increase in temperature, indicating the presence of a mineral in the tissue. Although diagram A follows the same pattern, the slope of the diagram is sharper due to less penetration of silver into the tissue, and only about 20% of the sample weight remains up to 100 °C.

### 3.7. Testes tissue histological and TUNEL studies

Evaluation of tissue sections in sham and control groups showed the normal structure of seminiferous tubules and interstitial connective tissue. The integrated germinal epithelium, including spermatogonia

(dark and close to the basement membrane), spermatocytes (primary and secondary), and spermatids (early, intermediate, and late), is located on the basement membrane, and the large and euchromatic nuclei of Sertoli cells can be observed. There are mature spermatozoa also in the lumen of the tubules. Leydig cells with large round nuclei and eosinophilic cytoplasm are located in the dense interstitial connective tissue (Fig. 12A-C). These findings indicate the normal distribution of cells in the testicular tissue of these groups. In the Ag 14 group, cavities were observed in the germinal epithelium and the interstitial tissue (vacuolation) despite the integrity of the basement membrane. The volume of interstitial connective tissue receded, while there was no tendency for the rupture of the epithelium, and the epithelium remained intact (Fig. 12D). In the Ag 35 group, the integrity of the epithelium and basement membrane was not evident in numerous tubules, and the cells of the germinal epithelium were separated from each other and the Sertoli cells by vacuoles. The number of germ cells and Sertoli cells and the thickness of the epithelium were lower than the control group. In some of the seminiferous tubules, the entire epithelium collapsed into the lumen of the tubes. More and larger cavities appeared in the interstitial tissue, and Leydig cells lessened (Fig. 12E-F). The results of the TUNEL assay showed a high rate of apoptotic cells in the lumen of seminiferous tubules and interstitial tissue of Ag14 and Ag35 groups compared to the sham and control groups (Fig. 13).

## 4. Discussion

Silver NPs have numerous advantages and applications in various fields, including medicine. However, they can also be toxic to germ cells. Studies have shown that the toxic effect of NPs depends on their size, chemical compound, concentration, effector pathway, exposure duration, and oxidative stress induction as the most common toxicity mechanism of NPs [40]. The range of the applications of NMs becomes broader when two or more metals are included in a single nanostructure. Among the bimetallic structures, Au@Ag core-shell NRs have better surface-enhanced Raman scattering (SERS) performance, the same lattice parameters, and the same surface energies (the surface energy of Ag is somewhat lower) [41,42]. In addition, Au NRs can serve as excellent carriers for forming silver shells [43]. No general study has evaluated the distribution of Au@Ag core-shell NRs with alginate coating in testicular tissue and their effects on sperm function. We investigated the synthesis and impacts of these nanostructures on testicular tissue and spermatozoa with this background in mind. One of the disadvantages of this synthesis method is the use of toxic substances, such as CTAB, which

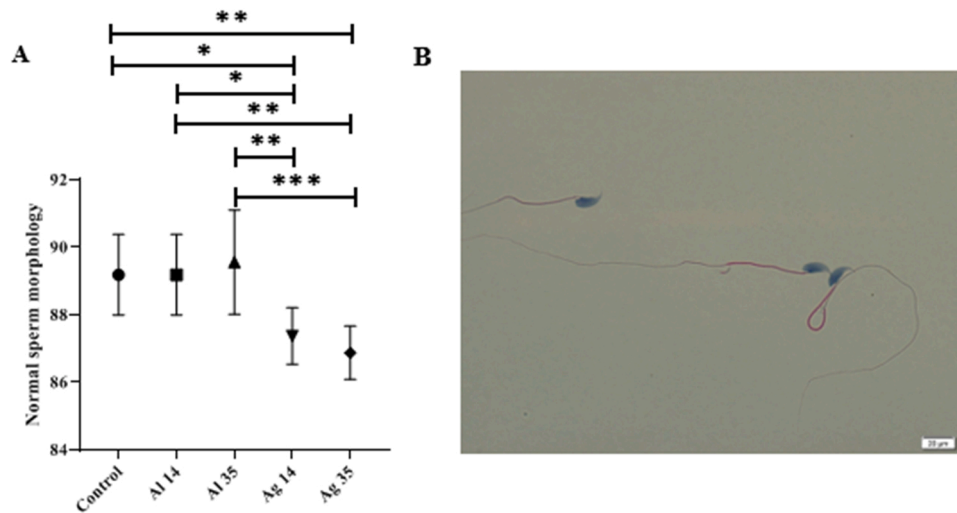


**Fig. 7.** The effect of nanostructure on sperm morphology in the experimental groups. (A) Comparison of sperm morphology between groups. (B) Examination of sperm morphology by Papanicolaou staining shows abnormal sperm in the groups that received nanostructure (×100). All results were expressed as mean ± SD (n = 8). \*P < 0.05, \* \*P < 0.01, and \* \* \*P < 0.001.

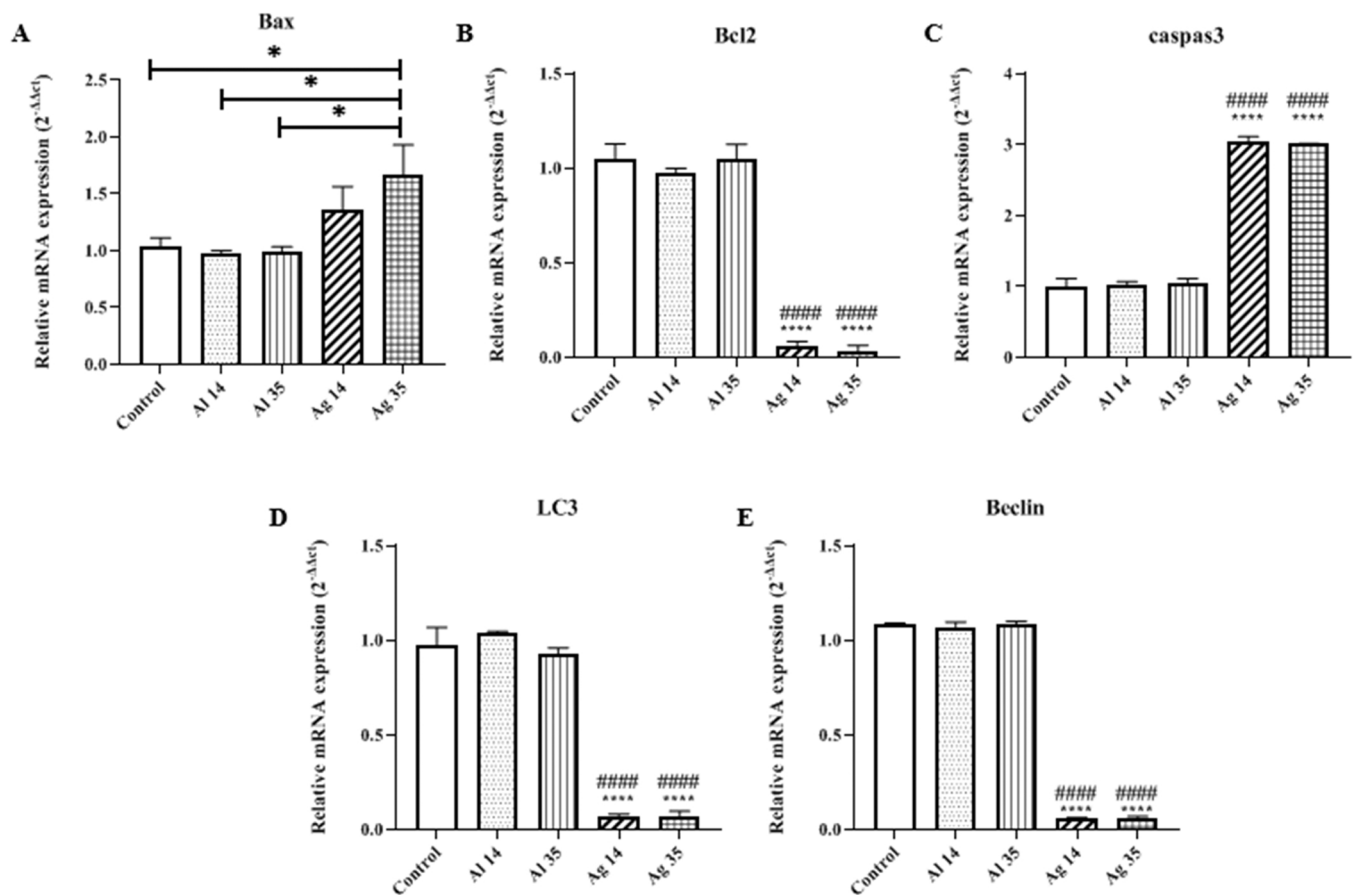


**Fig. 8.** The impacts of nanostructures on mRNA expression levels of Bax, Bcl-2, caspase-3, LC3, and Beclin-1. (A, C) The expression of Bax and caspase-3 was upregulated in the treatment groups and significantly increased compared with the other groups. (B) The expression of Bcl-2 decreased significantly in the Ag groups compared with the other groups. The expression levels of LC3 (D) and Beclin-1 (E) Show a significant decrease in the Ag14 and Ag35 groups compared with the other groups (n = 8) and β-actin was an internal control. \*P < 0.05, \* \* \* P < 0.0001 compared with the control group and ##### P < 0.0001 compared with the sham groups.

can damage cells. Therefore, we used a biocompatible coating called alginate to synthesize the nanostructures.

The results of characterizing the nanostructure showed that they are

mainly rod-shaped and have a core-shell structure. The particles are polydispersed (approximately 80% of the structures are rod-shaped, and 20% are spherical), and DLS evaluations confirmed this with a

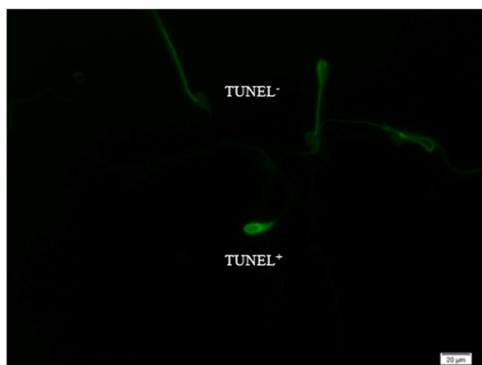


**Fig. 9.** TUNEL assay in Ag 35 group. Spermatozoa with a light green color are DNA fragmented (TUNEL<sup>+</sup>) and in contrast, spermatozoa with a pale green color are normal (TUNEL<sup>-</sup>) ( $\times 100$ ). scale bar = 20  $\mu$ m.

polydispersity index of 2.715. The mean of zeta potential of the resulting nanostructure before and after alginate coating changes from + 62.5 to - 62.4, indicating the successful modification of the coating. According

to UV–vis spectroscopy analysis, we should observe two peaks in NR structures. The first peak is near the infrared region with low intensity corresponding to the nanostructure diameter, and the second peak with high intensity near the ultraviolet region indicates the structure length. The optical absorption patterns of Au NRs, Au@Ag NRs, and Au@Ag NRs with alginate coating are consistent with this pattern, and the presence of two peaks in the UV nanostructure diagram demonstrates rod synthesis.

In a male mouse, the entire process of spermatocyte development, spermatid differentiation, and total spermatogenesis take about 14, 9, and 35 days, respectively. Moreover, the additional time in the epididymis is about one week until disulfide bonds are formed between adjacent protamines in the chromatin structure [44,45]. Consequently, we administered our injections to the mice for 2 and 5 weeks.

Sperms are specialized cells that provide half of the genetic material for the next generation by transferring it to the oocyte. Semen quality is considered an indicator of male fertility. Therefore, the evaluation of sperm parameters (semen analysis) is critical in treating infertility [46, 47]. According to our findings, progressive motility, total motility, sperm viability, count, and morphology were significantly lower than in the other groups ( $P < 0.0001$ ). It should be noted that most studies on

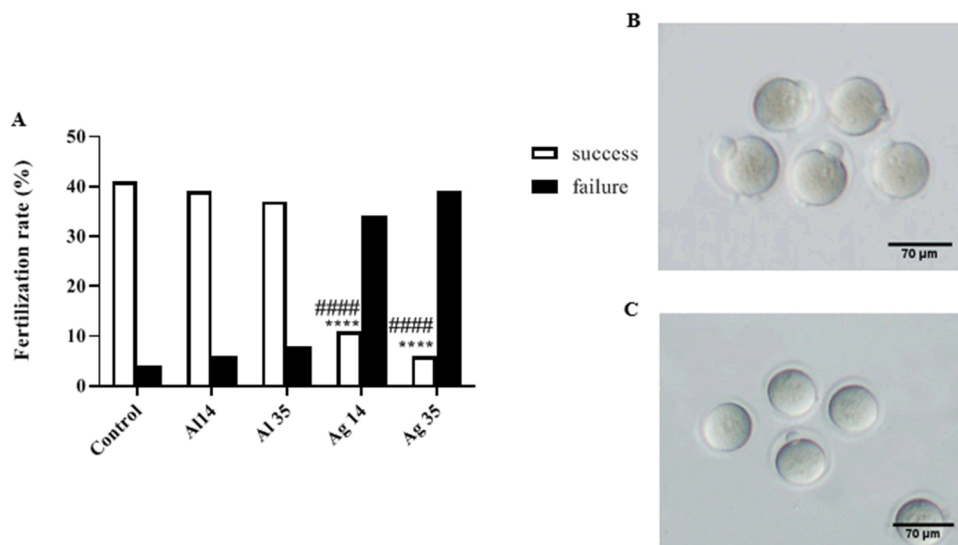


**Fig. 10.** The effect of nanostructures on fertilization rate in the groups. (A) There is a significant decrease in the treated groups compared to the control group ( $**** P < 0.0001$ ) and to the alginate group ( $#### P < 0.0001$ ). (B) Control group. (C) Ag 35 group. All results were expressed as mean  $\pm$  SD ( $n = 8$ ).

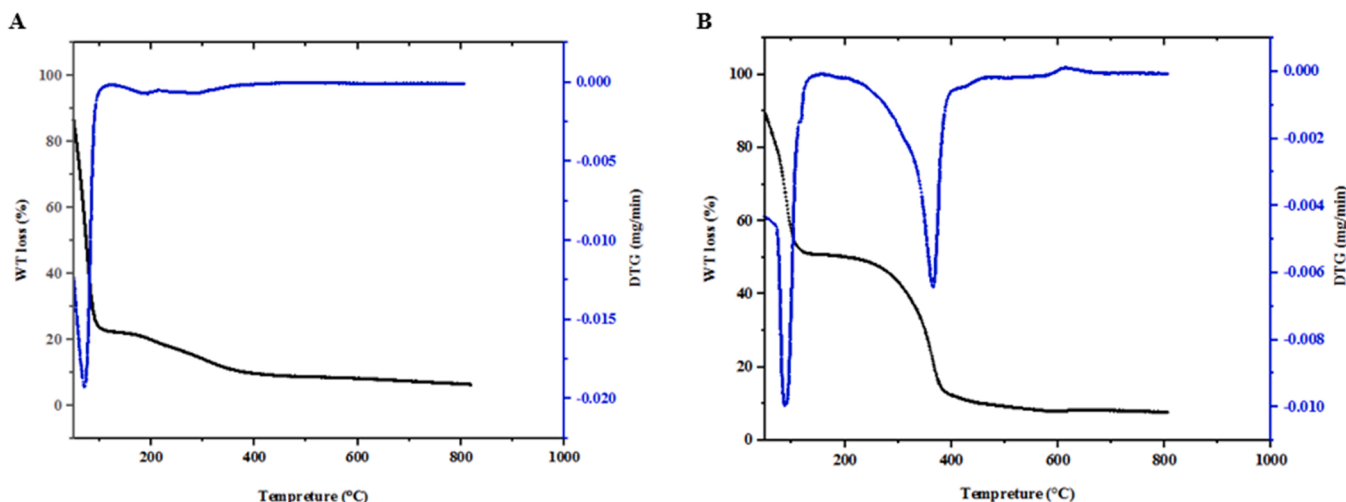


**Fig. 11.** TGA analysis. (A) Ag 14 and (B) Ag 35 groups.

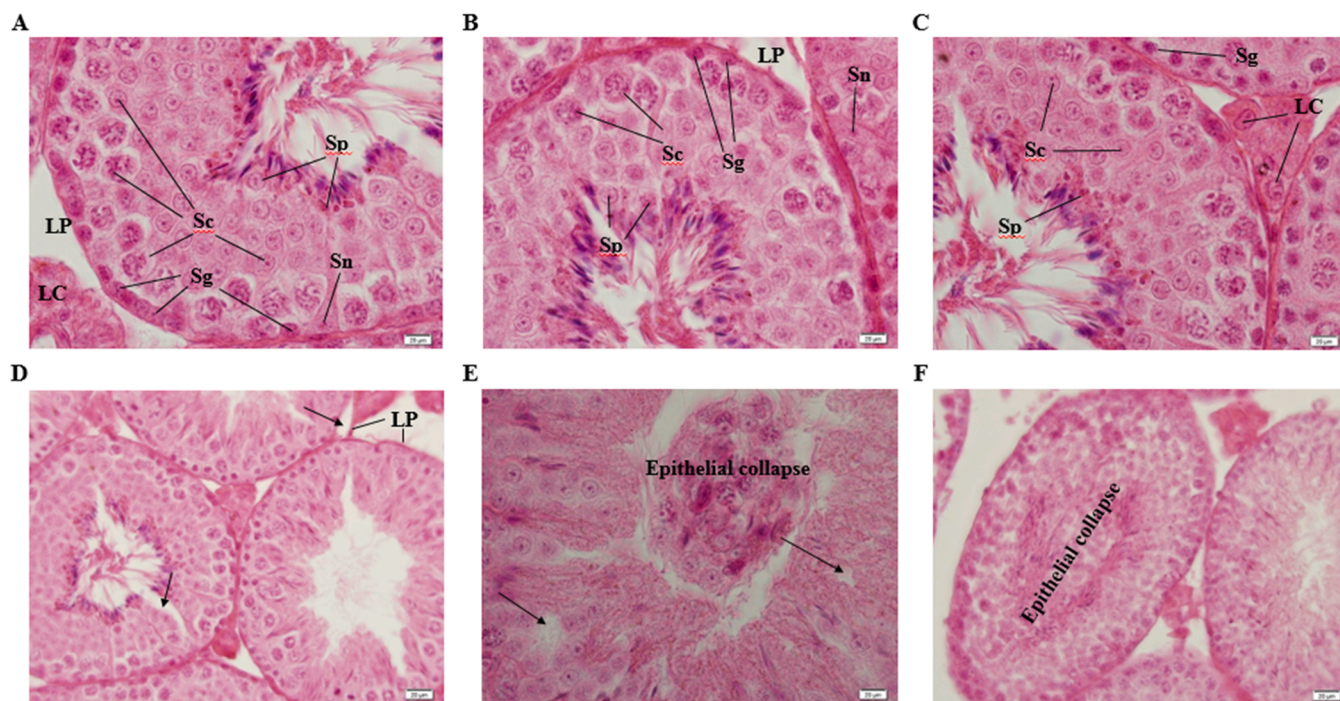


**Fig. 12.** Photomicrographs of testicular tissue stained with hematoxylin and eosin in the experimental groups (control - A, Al 14 - B, Al 35 - C, Ag 14 - D, and Ag 35 - E and F). (A-C) In the control and Al groups ( $\times 100$ ), normal structure and organization of testicular tubules and interstitial tissue were observed. (D) In the Ag 14 group ( $\times 40$ ), some cavities were observed in the germinal epithelium and interstitial tissue (arrows), but the basement membrane is intact. (E) In the Ag 35 group ( $\times 100$ ), the epithelium and basement membrane of numerous tubules are not intact, and cell separation of the germinal epithelium from each other and from Sertoli cells was observed. The number of germ cells and Sertoli cells and the thickness of the epithelium were reduced. (F) A release of germ cells into the lumen of the tubules was observed ( $\times 40$ ). LP, Lamina propria; Sn, Sertoli cell nucleus; Sg, Spermatogonia; Sc, spermatocyte; Sp, spermatid; LC, Leydig cell. scale bars = 20  $\mu$ m.

sperm parameters have been conducted with single metal NPs, such as gold, titanium dioxide, zinc, silver, and selenium [48–52].

In line with our results, Moretti et al. and Wiwanitkit et al. found that gold NPs and both gold and silver NPs reduced sperm motility in a dose-dependent manner [52,53]. Pawar et al. and Santonastaso et al. have also shown that titanium dioxide NPs affect sperm motility and viability [49,54]. In other studies, Abbasalipourkabir et al., de Brito et al., Arisha, and Ahmed et al. have reported that zinc oxide and silver NPs can decrease sperm quality and quantity factors, including morphology, motility, viability, and the number of sperms in rats, confirming our results [55–57].

Furthermore, the current study showed severe nonspecific sperm aggregation. Nonspecific sperm aggregation is the attachment of immotile sperms to other sperms, other cells, mucosal filaments, or debris [58]. Park et al. reported that Ag nanoparticles smaller than 71 nm in diameter (small NPs) could penetrate the blood-testes barrier (BTB) and accumulate in the testes. The proposed mechanism for BTB penetration involves an increase in the serum levels of *TGF- $\beta$*  and a subsequent rise in the serum levels of cytokines (e.g., *IL -1*, *IL -4*, *IL -6*, *IL -10*, and *IL -12*), distribution of B lymphocyte, and IgE production after administrating Ag NPs. This inflammatory response can weaken the integrity of the barrier [59]. In addition, Cheng et al. have shown that testosterone in interaction with *TGF- $\beta$*  can modulate the dynamics of crossing and BTB integration [60]. Based on our TGA analysis and histological results, the transfer of the nanostructures into the testicular tissue, penetration of the BTB, and increased Leydig cell apoptosis, leading to a decrease in serum testosterone levels, were confirmed. As a result, the possible mechanism for sperm aggregation is activating the inflammatory pathway, damage to BTB, and penetration of anti-sperm antibodies into the seminiferous tubules.

We examined mRNA expression to determine the effects of apoptotic and autophagy-regulating genes, such as *Bax*, *Bcl-2*, *caspase-3*, *LC3*, and *Beclin-1*, in spermatozoa exposed to nanostructure. Our q RT-PCR

findings demonstrated that nanostructure treatment upregulates the pro-apoptotic members of the *Bcl-2* family (*Bax*) and *caspase-3*. On the other hand, the anti-apoptotic members of this family, such as *Bcl-2* and autophagic markers (*Beclin-1* and *LC3*), were downregulated. Apoptosis and autophagy are two biological mechanisms that play an important role in tissue development and homeostasis. The interactions between the components of these two metabolic pathways suggest a complex interplay often triggered by similar stimuli, such as metabolic stress [12]. As a tumor suppressor protein activated by a range of stress conditions, *p53* regulates DNA repair mechanisms, *Bcl-2* family gene expression, and the apoptotic pathway [61]. Although many studies have demonstrated the role of *p53* in the apoptosis pathway, some report a strong connection between this protein and autophagy as *p53* activates AMP kinase and the subsequent inhibition of *mTOR*. The *mTOR* inhibition is thought to degrade *Bcl-2* and its homologs after nutrient deprivation and activate the autophagy pathway [12]. The *Bcl-2* family proteins are located in the mitochondria. These proteins have both pro-apoptotic (*Bax*, *Bak*, *Bim*, and *Bid*) and anti-apoptotic (*Bcl-2*, *Bcl-xl*, and *Bcl-w*) functions [9]. *Bcl-2*, as an anti-apoptotic protein, can inhibit the release of cytochrome C, an apoptotic factor, from mitochondria into the cytoplasm and control apoptosis and autophagy in a coordinated manner. On the other hand, *Beclin-1* is an autophagic marker involved in autophagosome formation. Studies have shown that the interaction between apoptosis and autophagy is affected by the interaction between anti-apoptotic members of the *Bcl-2* family and *Beclin-1* [12]. The *Bcl-2* / *Beclin-1* complex is located on the endoplasmic reticulum, which controls both apoptosis and autophagy, and also *Beclin-1* is considered a substrate for caspase. One of the important ubiquitin-like genes associated with autophagy is *Atg3*, an essential component of autophagosome formation. *Atg3* is a substrate for *caspase-8*, an initiator caspase of the apoptotic pathway during receptor-mediated cell death. Research has shown that autophagic activity is limited during apoptosis by the degradation of *Atg3* through death receptor stimulation and *caspase-8*

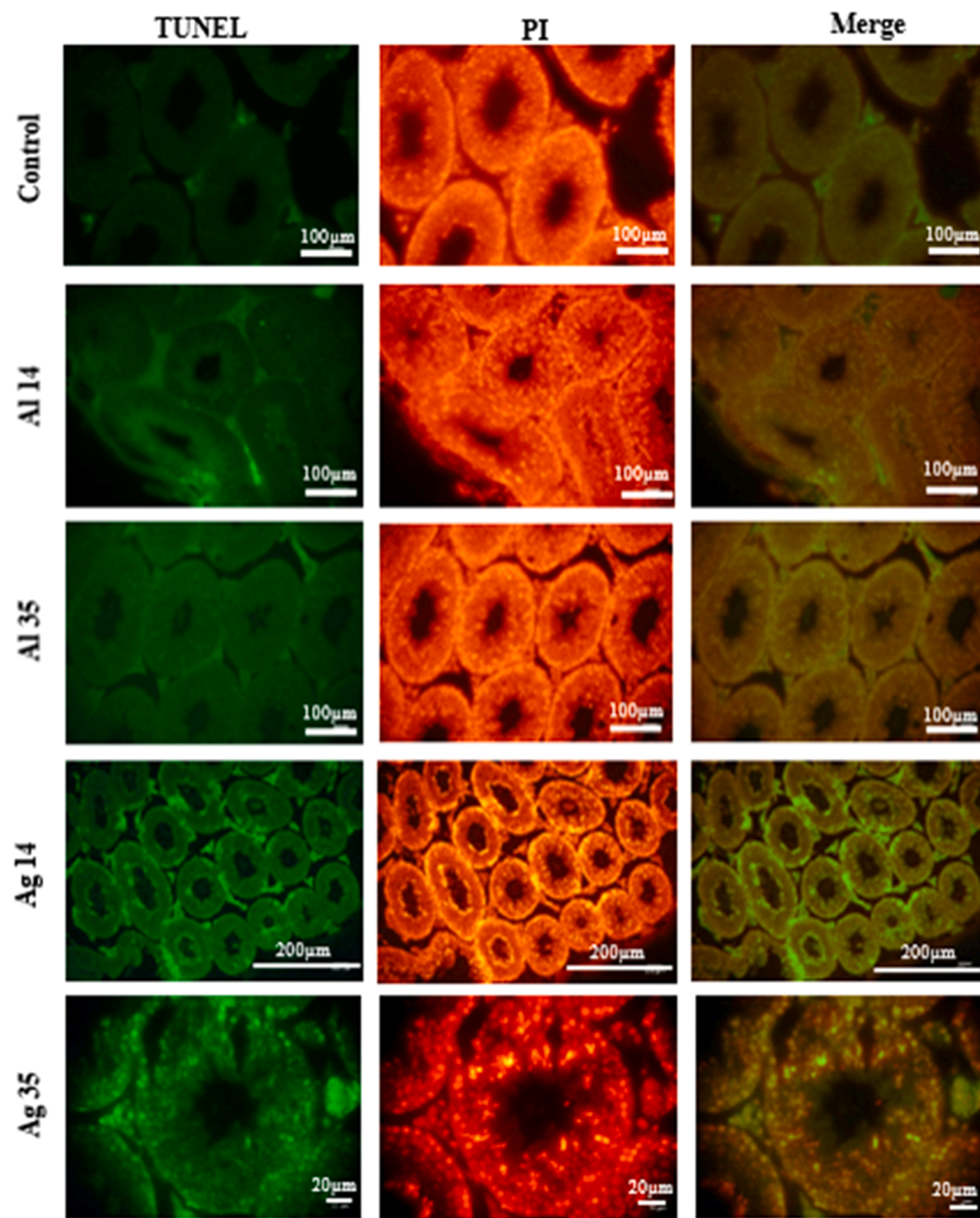


Fig. 13. Assessment of testicular cell apoptosis. TUNEL assay for testicular tissue shows TUNEL positive nuclei (green), indicating that apoptosis in germ cells is localized in testicular tubules and interstitial tissue. Differential staining of nuclei with PI. More apoptotic signals were received from Ag 35 group. Control, Al 14, and Al 35 scale bars = 100  $\mu\text{m}$  ( $\times 20$ ); Ag 14 scale bar = 200  $\mu\text{m}$  ( $\times 10$ ); Ag 35 scale bar = 20  $\mu\text{m}$  ( $\times 40$ ).

activation [62]. Moreover, in the apoptosis pathway, *Bax* promotes apoptosis by acting on voltage-gated ion channels in the mitochondrial membrane to release cytochrome C into the cytoplasm. *Caspase-3* is an endoprotease that plays an essential role as an apoptotic effector

molecule [63]. Stress factors in testicular tissue, such as toxic agents, can lead to an elevation in ROS and subsequently to the upregulation of *p53*, upregulation of *Bax* and *caspase-3*, and finally, to programmed cell death [64]. Sperms are prone to damage due to the high polyunsaturated fatty

acids and low antioxidant content [40]. Therefore, silver nanostructure as a stress factor raised ROS production and initiated the path of apoptosis via the above mechanisms.

The TUNEL assay has been used to detect DNA strand cleavages, the most important indication of sperm apoptosis. The results of this test confirm our findings on gene expression. Sperm DNA fragmentation may result in an inability to fertilize the oocyte and is associated with an increase in miscarriages [65]. Similar to our findings, Santonastaso et al. have shown that titanium dioxide NPs can augment DNA fragmentation in human spermatozoa [49]. No study has yet compared apoptosis and autophagy pathways in sperms exposed to nanostructures.

Our investigation has also demonstrated that the fertilization rate has significantly diminished, and sperms exposed to the nanostructure could not fertilize the oocytes. As mentioned above, sperm motility and viability decreased significantly in the mice treated with nanostructures, and strong aggregation was observed under the microscope. Gene expression and TUNEL assay results indicated apoptosis and sperm DNA fragmentation in these mice. Several studies have shown that fertilization occurs with DNA-damaged sperm, and the ability of the oocyte to repair the damaged paternal genome depends firstly on the genomic and cytoplasmic quality of the oocyte and secondly on the sperm DNA quality. However, the subsequent development of an embryo is impaired [37,66–68]. Therefore, the main reason for the decline in the fertility rate in our study was sperm aggregation and the resultant decrease in sperm motility.

Histological and TUNEL examinations of the testicular tissue revealed some time-dependent damage in seminiferous tubules in the treated groups, more pronounced in the Ag 35 group as a chronic phase. The images showed the reduced thickness of the germinal epithelium and the loss of its cohesion, as well as a reduction in the number of cells. These changes may be attributed to two main reasons. First, the inhibitory effect of Ag NSs on spermatogonial stem cells, and second, the extensive death of Sertoli cells, leading to vacuoles formation in the germinal epithelium. Studies indicated that silver NPs could decrease the activity of *FYN kinase*. This protein is a member of the *Src kinase* family and plays a role in spermatogonial proliferation. It also binds the spermatogenic cells to the Sertoli cells. Therefore, defects in its function and the inhibition of its activity cause the cells to detach from Sertoli cells [69]. According to the previous description, Ag-NSs cross the BTB and are oxidized by oxygen and other molecules in the tissue to release Ag<sup>+</sup>. These free ions can induce oxidative stress in cells and initiate apoptosis via intrinsic and extrinsic pathways by activating p53 [3,13]. The extrinsic pathway depends on death receptors, such as FAS. The testis is the richest tissue in the body in terms of the FAS ligand, and Sertoli cells that can express FAS ligand can induce the apoptosis of germinal epithelium cells with FAS receptors. On the other hand, a stress factor may cause Leydig cells to express numerous FAS receptors [13]. Our TUNEL results showed apoptotic signals from both seminiferous tubules and interstitial tissue. These findings suggest that the leading cause of sperm and spermatogenic cell death is the activation of intrinsic and extrinsic apoptotic pathways.

## 5. Conclusion

This study demonstrated that Au@Ag core-shell NRs with alginate coating negatively affected sperm function and testicular structure. It should be noted that some spherical particles were present in the final solution, which could have toxic effects on the reproductive system of mice. Therefore, due to the widespread use of nano-silver in everyday life and medicine, further investigations on the different forms of this structure and the reduction of its toxicity are of particular importance.

## Funding

The present study was supported by Iran University of Medical Sciences (IUMS) (NO. 98-3-4-15589).

## CRedit authorship contribution statement

**Mahsa Nazari:** Investigation, Methodology, Writing - original draft. **Ronak Shabani:** Investigation, Methodology. **Marziyeh Ajdary:** Software, review and editing. **Mohsen Ashjari:** Formal analysis. **Reza Shirazi:** Review and editing. **Azam Govahi:** Formal analysis. **Fatemeh Kermanian:** Review and editing. **Mehdi Mehdizadeh:** Project administration.

## Declaration of Competing Interest

The authors declare that they have no known competing financial interests or personal relationships that could have appeared to influence the work reported in this paper.

## Data Availability

Data will be made available on request.

## Acknowledgments

All experiments were performed in the laboratories of the Anatomy Department and Cellular and Molecular Research Center (CMRC), IUMS, Tehran, Iran.

## References

- [1] C. Ernst, et al., Staged developmental mapping and X chromosome transcriptional dynamics during mouse spermatogenesis, *Nat. Commun.* 10 (1) (2019) 1–20.
- [2] Y. Chen, et al., Single-cell RNA-seq uncovers dynamic processes and critical regulators in mouse spermatogenesis, *Cell Res.* 28 (9) (2018) 879–896.
- [3] S.M. Ahmed, S.A. Abdelrahman, S.M. Shalaby, Evaluating the effect of silver nanoparticles on testes of adult albino rats (histological, immunohistochemical and biochemical study), *J. Mol. Histol.* 48 (1) (2017) 9–27.
- [4] F. Asgari, et al., Risk of embryo aneuploidy is affected by the increase in sperm DNA damage in recurrent implantation failure patients under ICSI-CGH array cycles, *Hum. Fertil.* (2021) 1–9.
- [5] E. Kabartan, et al., Investigating the relationship between BRCA1 and BRCA2 genes methylation profile and sperm DNA fragmentation in infertile men, *Andrologia* 51 (7) (2019), e13308.
- [6] P. Zhang, et al., Low dose chlorothaloniol impairs mouse spermatogenesis through the intertwining of estrogen receptor pathways with histone and DNA methylation, *Chemosphere* 230 (2019) 384–395.
- [7] C.-Y. Liu, et al., Metformin ameliorates testicular function and spermatogenesis in male mice with high-fat and high-cholesterol diet-induced obesity, *Nutrients* 12 (7) (2020) 1932.
- [8] M. Honardoost, H. Soleimanjahi, F. Rajaei, Apoptosis: programmed cell death, *J. Inflamm. Dis.* 17 (3) (2013) 48–57.
- [9] M. Hassan, et al., Apoptosis and molecular targeting therapy in cancer, *BioMed. Res. Int.* 2014 (2014).
- [10] B. Macchi, et al., Role of inflammation and apoptosis in multiple sclerosis: comparative analysis between the periphery and the central nervous system, *J. Neuroimmunol.* 287 (2015) 80–87.
- [11] L. Murrow, J. Debnath, Autophagy as a stress-response and quality-control mechanism: implications for cell injury and human disease, *Annu. Rev. Pathol.: Mech. Dis.* 8 (2013) 105–137.
- [12] V. Nikolettou, et al., Crosstalk between apoptosis, necrosis and autophagy, *Biochim. Et. Biophys. Acta (BBA)-Mol. Cell Res.* 1833 (12) (2013) 3448–3459.
- [13] R. Opris, et al., Effects of silver nanoparticles functionalized with Cornus mas L. extract on architecture and apoptosis in rat testicle, *Nanomedicine* 14 (3) (2019) 275–299.
- [14] X.-F. Zhang, S. Gurunathan, J.-H. Kim, Effects of silver nanoparticles on neonatal testis development in mice, *Int. J. Nanomed.* 10 (2015) 6243.
- [15] M. Thakur, et al., Histopathological and ultra structural effects of nanoparticles on rat testis following 90 days (Chronic study) of repeated oral administration, *J. Nanobiotechnol.* 12 (1) (2014) 1–13.
- [16] C.M. Tollan, et al., Irreversible thermo-chromic behavior in gold and silver nanorod/polymeric ionic liquid nanocomposite films, *ACS Appl. Mater. Interfaces* 1 (2) (2009) 348–352.
- [17] E. Demir, A review on nanotoxicity and nanogenotoxicity of different shapes of nanomaterials, *J. Appl. Toxicol.* 41 (1) (2021) 118–147.
- [18] S. Dhiman, et al., Application of core/shell nanoparticles in smart farming: a paradigm shift for making the agriculture sector more sustainable, *J. Agric. Food Chem.* 69 (11) (2021) 3267–3283.
- [19] H.H. Dam, F. Caruso, Construction and degradation of polyrotaxane multilayers, *Adv. Mater.* 23 (27) (2011) 3026–3029.
- [20] F. Caruso, Nanoengineering of particle surfaces, *Adv. Mater.* 13 (1) (2001) 11–22.

- [21] K. Sakanishi, et al., Catalytic activity of NiMo sulfide supported on a particular carbon black of hollow microsphere in the liquefaction of a subbituminous coal, *Energy fuels* 10 (1) (1996) 216–219.
- [22] M.B. Gawande, et al., Core-shell nanoparticles: synthesis and applications in catalysis and electrocatalysis, *Chem. Soc. Rev.* 44 (21) (2015) 7540–7590.
- [23] J.K. Jaiswal, et al., Long-term multiple color imaging of live cells using quantum dot bioconjugates, *Nat. Biotechnol.* 21 (1) (2003) 47–51.
- [24] N. Sounderya, Y. Zhang, Use of core/shell structured nanoparticles for biomedical applications, *Recent Pat. Biomed. Eng.* 1 (1) (2008) 34–42.
- [25] P. De Farias, et al., Highly fluorescent semiconductor core-shell CdTe–CdS nanocrystals for monitoring living yeast cells activity, *Appl. Phys. A* 89 (4) (2007) 957–961.
- [26] L. Wei, et al., Silver nanoparticles: synthesis, properties, and therapeutic applications, *Drug Discov. Today* 20 (5) (2015) 595–601.
- [27] C.A. Dos Santos, et al., Silver nanoparticles: therapeutical uses, toxicity, and safety issues, *J. Pharm. Sci.* 103 (7) (2014) 1931–1944.
- [28] K. Durairaj, et al., Silver nanorods induced oxidative stress and chromosomal aberrations in the *Allium cepa* model, *IET Nanobiotechnol.* 14 (2) (2019) 161–166.
- [29] B. Nikoobakht, M.A. El-Sayed, Preparation and growth mechanism of gold nanorods (NRs) using seed-mediated growth method, *Chem. Mater.* 15 (10) (2003) 1957–1962.
- [30] W.H. Organization, World Health Statistics 2010, World Health Organization, 2010.
- [31] K. Narayana, An aminoglycoside antibiotic gentamycin induces oxidative stress, reduces antioxidant reserve and impairs spermatogenesis in rats, *J. Toxicol. Sci.* 33 (1) (2008) 85–96.
- [32] A. Hosseini, et al., Ameliorative effect of *Allium atroviolaceum* on sperm quality in cyclophosphamide-treated mice, *Future J. Pharm. Sci.* 7 (1) (2021) 1–11.
- [33] M. Rahimpour, et al., Effects of different doses of ethanol on sperm parameters, chromatin structure and apoptosis in adult mice, *Eur. J. Obstet. Gynecol. Reprod. Biol.* 170 (2) (2013) 423–428.
- [34] A. Govahi, et al., Accompaniment of time-lapse parameters and cumulus cell RNA-sequencing in embryo evaluation, *Reprod. Sci.* (2021) 1–15.
- [35] R.T. Schulte, et al., Sperm DNA damage in male infertility: etiologies, assays, and outcomes, *J. Assist. Reprod. Genet.* 27 (1) (2010) 3–12.
- [36] L. Gandini, et al., Study of apoptotic DNA fragmentation in human spermatozoa, *Hum. Reprod.* 15 (4) (2000) 830–839.
- [37] F. Horta, et al., Female ageing affects the DNA repair capacity of oocytes in IVF using a controlled model of sperm DNA damage in mice, *Hum. Reprod.* 35 (3) (2020) 529–544.
- [38] F. Mohammadi, et al., The effect of preincubation time and myo-inositol supplementation on the quality of mouse mii oocytes, *J. Reprod. Infertil.* 21 (4) (2020) 259.
- [39] Lahijani, M.S., et al., *Effects of quinazolinones on Balb/C mice embryonic livers.* 2011.
- [40] J. Gromadzka-Ostrowska, et al., Silver nanoparticles effects on epididymal sperm in rats, *Toxicol. Lett.* 214 (3) (2012) 251–258.
- [41] O. Kvitek, et al., Preparation of alloyed and “core-shell” Au/Ag bimetallic nanostructures on glass substrate by solid state dewetting, *J. Alloy. Compd.* 829 (2020), 154627.
- [42] P. Jiang, Y. Hu, G. Li, Biocompatible Au@ Ag nanorod@ ZIF-8 core-shell nanoparticles for surface-enhanced Raman scattering imaging and drug delivery, *Talanta* 200 (2019) 212–217.
- [43] L. Bi, et al., SERS-active Au@ Ag core-shell nanorod (Au@ AgNR) tags for ultrasensitive bacteria detection and antibiotic-susceptibility testing, *Talanta* 220 (2020), 121397.
- [44] J.M. Hutchison, D.C. Rau, J.E. DeRouchey, Role of disulfide bonds on DNA packaging forces in bull sperm chromatin, *Biophys. J.* 113 (9) (2017) 1925–1933.
- [45] I.D. Adler, Spermatogenesis and mutagenicity of environmental hazards: extrapolation of genetic risk from mouse to man, *Andrologia* 32 (4–5) (2000) 233–237.
- [46] R. Vidya, A. Saji, Naked eye detection of infertility based on sperm protamine-induced aggregation of heparin gold nanoparticles, *Anal. Bioanal. Chem.* 410 (13) (2018) 3053–3058.
- [47] U. Taylor, et al., Gold nanoparticles interfere with sperm functionality by membrane adsorption without penetration, *Nanotoxicology* 8 (1) (2014) 118–127.
- [48] A.R. Talebi, L. Khorsandi, M. Moridian, The effect of zinc oxide nanoparticles on mouse spermatogenesis, *J. Assist. Reprod. Genet.* 30 (9) (2013) 1203–1209.
- [49] M. Santonastaso, et al., In vitro genotoxic effects of titanium dioxide nanoparticles (n-TiO<sub>2</sub>) in human sperm cells, *Mol. Reprod. Dev.* 86 (10) (2019) 1369–1377.
- [50] M.A. Rezvanfar, et al., Protection of cisplatin-induced spermatotoxicity, DNA damage and chromatin abnormality by selenium nano-particles, *Toxicol. Appl. Pharmacol.* 266 (3) (2013) 356–365.
- [51] M. Nazar, et al., Acute and chronic effects of gold nanoparticles on sperm parameters and chromatin structure in Mice, *Int. J. Reprod. Biomed.* 14 (10) (2016) 637.
- [52] E. Moretti, et al., In vitro effect of gold and silver nanoparticles on human spermatozoa, *Andrologia* 45 (6) (2013) 392–396.
- [53] V. Wiwanitkit, A. Sereemasun, R. Rojanathanes, Effect of gold nanoparticles on spermatozoa: the first world report, *Fertil. Steril.* 91 (1) (2009) e7–e8.
- [54] K. Pawar, G. Kaul, Toxicity of titanium oxide nanoparticles causes functionality and DNA damage in buffalo (*Bubalus bubalis*) sperm in vitro, *Toxicol. Ind. Health* 30 (6) (2014) 520–533.
- [55] J.L.M. de Brito, et al., Acute reproductive toxicology after intratesticular injection of silver nanoparticles (AgNPs) in Wistar rats, *Nanotoxicology* 14 (7) (2020) 893–907.
- [56] A.H. Arisha, et al., Morin ameliorates the testicular apoptosis, oxidative stress, and impact on blood–testis barrier induced by photo-extracellularly synthesized silver nanoparticles, *Environ. Sci. Pollut. Res.* 26 (28) (2019) 28749–28762.
- [57] R. Abbasalipourkabir, et al., Toxicity of zinc oxide nanoparticles on adult male Wistar rats, *Food Chem. Toxicol.* 84 (2015) 154–160.
- [58] R. De Celis, et al., Semen quality of workers occupationally exposed to hydrocarbons, *Fertil. Steril.* 73 (2) (2000) 221–228.
- [59] E.-J. Park, et al., Repeated-dose toxicity and inflammatory responses in mice by oral administration of silver nanoparticles, *Environ. Toxicol. Pharmacol.* 30 (2) (2010) 162–168.
- [60] C.Y. Cheng, et al., Regulation of spermatogenesis in the microenvironment of the seminiferous epithelium: new insights and advances, *Mol. Cell. Endocrinol.* 315 (1–2) (2010) 49–56.
- [61] H. Azimian, et al., Bax/Bcl-2 expression ratio in prediction of response to breast cancer radiotherapy, *Iran. J. Basic Med. Sci.* 21 (3) (2018) 325.
- [62] O. Oral, et al., Cleavage of Atg3 protein by caspase-8 regulates autophagy during receptor-activated cell death, *Apoptosis* 17 (8) (2012) 810–820.
- [63] Z. Changizi, et al., Chlorogenic acid induces 4T1 breast cancer tumor’s apoptosis via p53, Bax, Bcl-2, and caspase-3 signaling pathways in BALB/c mice, *J. Biochem. Mol. Toxicol.* 35 (2) (2021), e22642.
- [64] P. Kielbik, et al., Transfer of orally administered ZnO: Eu nanoparticles through the blood–testis barrier: the effect on kinetic sperm parameters and apoptosis in mice testes, *Nanotechnology* 30 (45) (2019), 455101.
- [65] G. Ruvolo, et al., New molecular markers for the evaluation of gamete quality, *J. Assist. Reprod. Genet.* 30 (2) (2013) 207–212.
- [66] D. Sakkas, J.G. Alvarez, Sperm DNA fragmentation: mechanisms of origin, impact on reproductive outcome, and analysis, *Fertil. Steril.* 93 (4) (2010) 1027–1036.
- [67] F. Marchetti, et al., Meiotic interstrand DNA damage escapes paternal repair and causes chromosomal aberrations in the zygote by maternal misrepair, *Sci. Rep.* 5 (1) (2015) 1–7.
- [68] R.J. Aitken, et al., Causes and consequences of oxidative stress in spermatozoa, *Reprod. Fertil. Dev.* 28 (2) (2016) 1–10.
- [69] S.M. Miresmaeili, et al., Evaluating the role of silver nanoparticles on acrosomal reaction and spermatogenic cells in rat, *Iran. J. Reprod. Med.* 11 (5) (2013) 423.